Characterization of β-Sheet Structure in Ure2p$_{1-89}$ Yeast Prion Fibrils by Solid-State Nuclear Magnetic Resonance†

Ulrich Baxa,‡ Reed B. Wickner,§ Alasdair C. Steven,‡ D. Eric Anderson,|| Lyuben N. Marekov,‡ Wai-Ming Yau,⊥ and Robert Tycko*,⊥

Laboratory of Structural Biology, National Institute of Arthritis, Musculoskeletal, and Skin Diseases, National Institutes of Health, Bethesda, Maryland 20892-8025, Laboratory of Biochemistry and Genetics, National Institute of Diabetes and Digestive and Kidney Diseases, National Institutes of Health, Bethesda, Maryland 20892-0830, Proteomics and Mass Spectrometry Facility, National Institute of Diabetes and Digestive and Kidney Diseases, National Institutes of Health, Bethesda, Maryland 20892-0810, and Laboratory of Chemical Physics, National Institute of Diabetes and Digestive and Kidney Diseases, National Institutes of Health, Bethesda, Maryland 20892-0520

Received May 1, 2007; Revised Manuscript Received September 11, 2007

ABSTRACT: Residues 1−89 constitute the Asn- and Gln-rich segment of the Ure2p protein and produce the [URE3] prion of *Saccharomyces cerevisiae* by forming the core of intracellular Ure2p amyloid. We report the results of solid-state nuclear magnetic resonance (NMR) measurements that probe the molecular structure of amyloid fibrils formed by Ure2p$_{1-89}$ *in vitro*. Data include measurements of intermolecular magnetic dipole−dipole couplings in samples that are ^{13}C-labeled at specific sites and two-dimensional ^{15}N−^{13}C and ^{13}C−^{13}C NMR spectra of samples that are uniformly ^{15}N- and ^{13}C-labeled. Intermolecular dipole−dipole couplings indicate that the β-sheets in Ure2p$_{1-89}$ fibrils have an in-register parallel structure. An in-register parallel β-sheet structure permits polar zipper interactions among side chains of Gln and Asn residues and explains the tolerance of [URE3] to scrambling of the sequence in residues 1−89. Two-dimensional NMR spectra of uniformly labeled Ure2p$_{1-89}$ fibrils, even when fully hydrated, show NMR linewidths that exceed those in solid-state NMR spectra of fibrils formed by residues 218−289 of the HET-s prion protein of *Podospora anserina* [as originally reported in Siemer, A. B., Ritter, C., Ernst, M., Riek, R., and Meier, B. H. (2005) *Angew. Chem., Int. Ed. 44,* 2441−2444 and confirmed by measurements reported here] by factors of three or more, indicating a lower degree of structural order at the molecular level in Ure2p$_{1-89}$ fibrils. The very high degree of structural order in HET-s fibrils indicated by solid-state NMR data is therefore not a universal characteristic of prion proteins, and is likely to be a consequence of the evolved biological function of HET-s in heterokaryon incompatibility. Analysis of cross peak intensities in two-dimensional NMR spectra of uniformly labeled Ure2p$_{1-89}$ fibrils suggests that certain portions of the amino acid sequence may not participate in a rigid β-sheet structure, possibly including portions of the Asn-rich segment between residues 44 and 76.

The [URE3] prion of *Saccharomyces cerevisiae* is an infectious intracellular aggregated form of the Ure2p protein, with the morphological, tinctorial, and molecular structural characteristics of an amyloid fibril (*1*−*4*). In the [URE3] state, *Saccharomyces cerevisiae* cells are able to utilize ureidosuccinate in place of uracil in the presence of ammonia. In the more common [ure-o] state, corresponding to the absence of intracellular Ure2p amyloid, utilization of ureidosuccinate is blocked in the presence of ammonia (*5*). Unaggregated Ure2p acts by inhibiting the transcription factor Gln3p (reviewed in ref (*6*)). Current interest in [URE3] and other fungal prions (reviewed in ref (*7*)) arises in part from the fact that these prions are more amenable to experimentation and manipulation than are the mammalian prions that are associated with transmissible spongiform encephalopathies. Generation of [URE3] from recombinant Ure2p aggregated *in vitro* proves that [URE3] is a protein-only trait (*8*). Strains or variants of [URE3] and other yeast prions have been identified and attributed to self-propagating variations in the molecular structure of the amyloid fibrils (*8*−*13*).

The C-terminal domain of Ure2p (residues 97−354) is primarily responsible for the normal function of Ure2p as a regulator of nitrogen catabolism (*3*). The full molecular structure of the C-terminal domain has been determined by X-ray crystallography and is similar to that of glutathione S-transferases (*14*, *15*). The N-terminal domain of Ure2p (residues 1−89, or Ure2p$_{1-89}$) has an Asn-rich (33 out of

† Supported by the Intramural Research Programs of the National Institute of Arthritis, Musculoskeletal, and Skin Diseases and the National Institute of Diabetes and Digestive and Kidney Diseases, National Institutes of Health.

* Corresponding author. National Institutes of Health, Building 5, Room 112, Bethesda, MD 20892-0520. Phone: 301-402-8272. Fax: 301-496-0825. E-mail: robertty@mail.nih.gov.

‡ Laboratory of Structural Biology, National Institute of Arthritis, Musculoskeletal, and Skin Diseases.

§ Laboratory of Biochemistry and Genetics, National Institute of Diabetes and Digestive and Kidney Diseases.

|| Proteomics and Mass Spectrometry Facility, National Institute of Diabetes and Digestive and Kidney Diseases.

⊥ Laboratory of Chemical Physics, National Institute of Diabetes and Digestive and Kidney Diseases.

10.1021/bi700826b This article not subject to U.S. Copyright. Published 2007 by the American Chemical Society
Published on Web 10/23/2007

89 residues) and, to a lesser extent, Gln-rich (10 out of 89 residues) sequence. Ure2p$_{1-89}$ and shorter fragments of the N-terminal domain have been shown to form amyloid fibrils *in vitro* and to induce [URE3] when overexpressed in *S. cerevisiae* (*1*, *3*). Deletion of residues 1−65 from Ure2p abrogates [URE3] propagation, and these residues constitute the most protease-resistant part of Ure2p amyloid (*16*). Fusion of the Ure2p$_{1-89}$ sequence to the N-termini of several enzymes with globular structures results in amyloid fibrils with essentially full enzymatic activity, implying that the globular domains are not perturbed by amyloid aggregation (*17*, *18*). Thus, Ure2p$_{1-89}$ contains the "prion domain" of Ure2p.

Amyloid fibrils are β-sheet-rich filamentous aggregates that are formed by many peptides and proteins. As shown by X-ray fiber diffraction (*19*), and supported by electron microscopy (*20*), electron diffraction (*10*, *21*), and solid-state nuclear magnetic resonance (NMR[1]) (*22*), the β-sheets in an amyloid fibril have a "cross-β" orientation, meaning that the β-strand segments that form the sheets run approximately perpendicular to the long axis of the fibril, while the interstrand backbone hydrogen bonds in the sheets are approximately parallel to the long axis. Solid-state NMR measurements have been particularly valuable in distinguishing parallel (*23*−*30*) from antiparallel (*31*−*35*) β-sheets in amyloid fibrils and in elucidating other molecular-level structural features, leading to experimentally based models for amyloid structures at various levels of detail (*26*, *27*, *31*, *36*−*45*). In the case of fibrils formed by the β-amyloid peptide associated with Alzheimer's disease, full molecular models have been developed from solid-state NMR data in combination with constraints from electron microscopy (*41*).

Solid-state NMR measurements on fibrils formed by residues 10−39 of Ure2p (Ure2p$_{10-39}$) (*26*), the most highly conserved segment of the prion domain (*46*), have shown that these fibrils contain in-register, parallel β-sheets and that intermolecular interactions among side chain amide groups of Gln residues may be important in stabilizing the fibril structure, as originally proposed by Perutz for polyGln fibrils (*47*). Intermolecular interactions among side chain amide groups of Asn residues may also be important, as seen in the crystal structure of the peptide GNNQQNY (representing residues 7−13 of the Sup35 prion protein) reported by Nelson et al. (*48*). Ross et al. have shown that scrambling the sequence of the prion domain of Ure2p, while preserving the amino acid composition, does not prevent prion formation *in vivo* (*49*). This surprising result can be understood if the prion domain adopts an in-register, parallel β-sheet structure in Ure2p fibrils, stabilized by intermolecular interactions among Gln (and possibly Asn) residues or by other interactions among like residues, as demonstrated by Chan et al. for Ure2p$_{10-39}$ fibrils (*26*). However, direct experimental data on the β-sheet structure in fibrils formed by the full-length Ure2p prion domain (i.e., Ure2p$_{1-89}$) have not been reported previously. Ure2p$_{1-89}$ fibrils prepared *in vitro* have been shown to induce [URE3] in *S. cerevisiae*, while induction of [URE3] by Ure2p$_{10-39}$ fibrils has not been achieved (*8*), raising the possibility that the β-sheet structures may be different in the two cases.

In this paper, we report the results of solid-state NMR measurements designed to determine whether Ure2p$_{1-89}$ fibrils have the same in-register parallel β-sheet structure found in Ure2p$_{10-39}$ fibrils (*26*) and in fibrils formed by Sup35NM, which comprises the [PSI] prion of *S. cerevisiae* (*25*). The measurements are performed on fibrils prepared *in vitro* from recombinant Ure2p$_{1-89}$, expressed in *Escherichia coli* and ^{13}C-labeled at backbone carbonyl sites of either all Leu or all Val residues, or at methyl carbon sites of Ala residues. Data described below demonstrate that Ure2p$_{1-89}$ fibrils do indeed contain in-register parallel β-sheets. In addition, we report the results of solid-state NMR measurements on fibrils that are uniformly ^{15}N,^{13}C-labeled. Measurements on uniformly labeled Ure2p$_{1-89}$ fibrils are motivated in part by the success of recent solid-state NMR studies of fibrils formed by the prion domain of the HET-s prion of *Podospora anserina* (*42*, *50*, *51*), which indicate an unusually high degree of structural order in HET-s fibrils compared with the degree of order in β-amyloid (*27*, *41*, *52*) or other nonprion amyloid fibrils (*53*). Data described below show that Ure2p$_{1-89}$ fibrils are not as highly ordered as HET-s fibrils, implying that the high degree of structural order in HET-s fibrils is not a general feature of prions but instead is a likely consequence of the evolved, biologically functional nature of HET-s fibrils, as suggested previously by Ritter et al. (*42*). Solid-state NMR data for uniformly labeled Ure2p$_{1-89}$ fibrils also suggest that, contrary to our expectations, the Asn-rich segments of Ure2p$_{1-89}$ may not participate entirely in immobile β-sheets.

MATERIALS AND METHODS

Expression, Labeling, and Fibrillization of Ure2p$_{1-89}$. His-tagged Ure2p$_{1-89}$ (i.e., MHHHHHH-Ure2p$_{1-89}$) was expressed in *E. coli* BL21 from the expression vector pKT55 (*16*). For the preparation of site-specific labeled Ure2p$_{1-89}$ (Leu-^{13}CO-Ure2p$_{1-89}$, Val-^{13}CO-Ure2p$_{1-89}$, Ala-^{13}CH$_3$-Ure2p$_{1-89}$, and Arg-^{13}CO-Ure2p$_{1-89}$) a published protein expression protocol (*54*) was used with minor modifications. A culture was grown overnight in 10 mL of LB$_{amp}$ broth. Cells were harvested by centrifugation, taken up in 2 mL of water, and used to inoculate a synthetic medium with a composition essentially as described by Cai et al. (*55*), supplemented with 100 mg/L of each of the 20 amino acids (without isotopic labels, to inhibit biosynthesis) and 100 mg/L ampicillin. The culture was grown at 37 °C to an optical density of 0.8 at 600 nm. Cells were harvested by centrifugation and resuspended in the same volume of fresh prewarmed synthetic medium, again supplemented with 100 mg/L of each of the 20 amino acids, but with the desired ^{13}C-labeled amino acids in place of the corresponding unlabeled amino acids (also 100 mg/L, except 1 g/L of labeled alanine in the case of Ala-^{13}CH$_3$-Ure2p$_{1-89}$). After 15 min of further growth, expression of Ure2p$_{1-89}$ was induced by addition of 1 mM IPTG for a period of 4 h. Note that the medium for preparation of Leu-^{13}CO-Ure2p$_{1-89}$ included methyl-labeled alanine at 100 mg/L, but incorporation of labeled alanine in this sample was later determined to be too low to produce interpretable solid-state NMR data

[1] Abbreviations: NMR, nuclear magnetic resonance; GdnHCl, guanidine hydrochloride; 2D, two-dimensional; SDS, sodium dodecyl sulfate; 1D, one-dimensional; TEM, transmission electron microscope; MAS, magic-angle spinning; fpRFDR-CT, constant-time finite-pulse radiofrequency-driven recoupling; CSA, chemical shift anisotropy.

(see below), necessitating the preparation of a separate Ala-$^{13}CH_3$-Ure2p$_{1-89}$ sample.

For the preparation of uniformly ^{15}N,^{13}C-labeled Ure2p$_{1-89}$ (U-^{15}N,^{13}C-Ure2p$_{1-89}$), a 10 mL overnight culture in LB$_{amp}$ broth was harvested, washed twice in water, and used to inoculate a minimal medium enriched with trace elements (13 g/L KH_2PO_4, 10 g/L K_2HPO_4, 9 g/L Na_2HPO_4, 1 g/L U-^{15}N-NH_4Cl, 4 g/L U-^{13}C-glucose, 10 mM $MgSO_4$, 0.03 g/L thiamine, 0.6 mg/L $FeSO_4$, 0.6 mg/L $CaCl_2$, 0.12 mg/L $MnCl_2$, 0.08 mg/L $CoCl_2$, 0.07 mg/L $ZnSO_4$, 0.03 mg/L $CuCl_2$, 2.0 μg/L H_3BO_3, 0.025 mg/L $(NH_4)_6Mo_7O_{24}$, 0.5 mg/L EDTA, 100 mg/L ampicillin). Cultures were grown to an optical density of 0.8 at 600 nm before expression of Ure2p$_{1-89}$ was induced by the addition of 1 mM IPTG. Cultures were grown for an additional 12 h at 37 °C to a final optical density of about 2.5 at 600 nm before cells were harvested.

Ure2p$_{1-89}$ was purified using Ni-NTA agarose (Qiagen) under denaturing conditions with the batch method according to the recommendations of the manufacturer. Briefly, cells were lysed by gentle agitation for 30 min at room temperature in 6 M guanidine hydrochloride (GdnHCl) in 100 mM sodium phosphate, 10 mM Tris, pH 8.0 (buffer A). The cell lysate was cleared by centrifugation at 40000*g* for 1 h. Ni-NTA agarose resin was added to the supernatant and incubated under soft agitation for 1 h. The agarose was loaded in a column, washed with 8 M urea in 100 mM sodium phosphate, 10 mM Tris, pH 8.0, washed again with 8 M urea in 100 mM sodium phosphate, 10 mM Tris, pH 6.3, and finally eluted with 200 mM imidazole in 8 M urea, 100 mM sodium phosphate, 10 mM Tris, pH 4.5. Eluted fractions were analyzed by SDS−PAGE and stored at −70 °C.

Fibril formation was induced by dialysis of Ure2p$_{1-89}$ fractions against 2 mM sodium phosphate, pH 7.0. Fibrils formed during dialysis. In an attempt to increase the level of structural order in U-^{13}C,^{15}N-Ure2p$_{1-89}$ fibrils (and thereby decrease the solid-state NMR linewidths), we also tested a gradual dialysis scheme in which eluted fractions were dialyzed against buffer containing decreasing urea concentrations (7.0 M, 6.5 M, 6.0 M, 5.5 M, 5.0 M, and 4.0 M for 16 h, 8 h, 16 h, 8 h, 16 h, and 8 h, respectively, followed by final dialysis at 0 M urea). The first visible precipitation was observed between 5.5 and 5.0 M urea. However, gradual dialysis did not affect the level of structural order, as determined from linewidths in two-dimensional (2D) solid state $^{13}C-^{13}C$ NMR spectra, or any other aspects of the 2D spectra. Importantly, this protocol for fibril formation is not significantly different from the protocol used by Brachmann et al. to prepare infectious Ure2p$_{1-89}$ fibrils (*8*), in which Ure2p$_{1-89}$ was also His-tagged, purified and eluted under denaturing conditions with a Ni-NTA resin, and fibrillized by dialysis against buffer without denaturant.

Isotopic enrichment was quantified by mass spectrometry. Aliquots of labeled and unlabeled filaments were pelleted and redissolved in sodium dodecyl sulfate (SDS) buffer with 10 M urea, boiled for 2 min, and run on SDS−PAGE gels. After colloidal Coomassie staining, the Ure2p$_{1-89}$ band was excised. For site-specifically labeled peptides the bands were subjected to in-gel trypsin digestion. Mass spectra were obtained with a Waters CapLC/QTOF-2 instrument, using a microscale C18 column. In the case of Leu-^{13}CO-Ure2p$_{1-89}$, the peptide MMNNNGNQVSNLSNALR was used for analysis by further fragmentation. The isotope distribution for the SNALR ion was shifted by 1 Da relative to that of the same ion in the unlabeled sample, while the isotope distribution of the SNA ion exhibited only minor differences. Isotopic enrichments were calculated to be approximately 31% for $^{13}CH_3$ of alanine and 92% for ^{13}CO of leucine in Leu-^{13}CO-Ure2p$_{1-89}$, consistent with the solid-state NMR spectra discussed below. The high enrichment for leucine was also confirmed by the isotope distribution of the LR ion. For Val-^{13}CO-Ure2p$_{1-89}$ and Arg-^{13}CO-Ure2p$_{1-89}$ the isotope distribution of the peptide QVNIGNR was used to estimate isotopic enrichment. Isotopic enrichments were approximately 75% for ^{13}CO of valine in Val-^{13}CO-Ure2p$_{1-89}$ and ∼33% for ^{13}CO of arginine in Arg-^{13}CO-Ure2p$_{1-89}$. Solid state ^{13}C NMR measurements of carbonyl signals from Arg-^{13}CO-Ure2p$_{1-89}$ and methyl signals from Leu-^{13}CO-Ure2p$_{1-89}$ were attempted but could not be analyzed due to the low isotopic enrichment. Measurements on carbonyl signals in Leu-^{13}CO-Ure2p$_{1-89}$ and Val-^{13}CO-Ure2p$_{1-89}$ and on methyl signals in Ala-$^{13}CH_3$-Ure2p$_{1-89}$ are discussed below.

For U-^{15}N,^{13}C-Ure2p$_{1-89}$, tryptic digests were analyzed on an Applied Biosystems Voyager DE-Pro time-of-flight mass spectrometer in the reflectron mode. Isotopic enrichment was estimated to be greater than 98%, and no variations in the levels of enrichment of different amino acids were observed. In particular, Asn and Gln residues were found to have ^{13}C enrichment levels greater than 98%.

For ^{13}CO-labeled Ure2p$_{1-89}$, scrambling of ^{13}CO labels was assessed by solution ^{13}C NMR spectroscopy of acid-hydrolyzed samples. Approximately 4 mg of peptide was dissolved in 1 mL of a 1:1 mixture of HCl and propionic acid, heated to 150 °C for 30 min in sealed, evacuated ampules, and dried under a continuous stream of dry nitrogen gas. Hydrolyzed material was then dissolved in ammonium carbonate buffer, filtered through a 0.2 μm filter, and lyophilized. The resulting powder was dissolved in 0.5 mL of 10% D_2O/90% H_2O and adjusted to pH 7.8 with dilute HCl and NaOH. Proton-decoupled ^{13}C NMR spectra were obtained on a Varian Mercury spectrometer and compared with reference spectra of corresponding ^{13}C-labeled amino acids. No carboxylate ^{13}C NMR lines attributable to scrambling of ^{13}CO labels were detected in Leu-^{13}CO-Ure2p$_{1-89}$ and Val-^{13}CO-Ure2p$_{1-89}$ samples (detection threshold approximately 5%, limited by signal-to-noise in the ^{13}C NMR spectra).

Additional details of mass spectrometry and solution NMR are given in Supporting Information.

Preparation of Synthetic Peptides. The peptides Ac-NNNNNSSSNNNN-NH_2 and Ac-QQQQQQSSSQQQQ-NH_2 (with acetyl and amide capping groups at the N- and C-termini, respectively) were synthesized by standard FMOC protocols on an Applied Biosystems model 433A automated solid-phase peptide synthesizer. After cleavage from the synthesis resin, precipitation in cold *t*-butyl methyl ether, resuspension in water, and lyophilization, the crude peptides were dissolved in trifluoroacetic acid at a concentration of approximately 15 mM (based on crude peptide weight), diluted to a concentration of approximately 270 μM in 6 M guanidine hydrochloride (GdnHCl), and adjusted to pH 6.5−8.0 by addition of concentrated NaOH and phosphate buffer. GdnHCl was subsequently removed by fast protein liquid

chromatography, using a desalting column (HiTrap, GE Healthcare) equilibrated with 10 mM phosphate buffer, pH 7.0, containing 0.01% NaN_3 to inhibit bacterial and fungal growth. For Ac-NNNNNSSSNNNN-NH_2, the peptide concentration in this buffer after removal of GdnHCl was approximately 35 μM. Aliquots of the Ac-NNNNNSSSNNNN-NH_2 solution were concentrated by factors of 4 and 16 by centrifugal evaporation. Aggregation of Ac-NNNNNSSSNNNN-NH_2 at 35 μM, 140 μM, and 560 μM concentrations was monitored by electron microscopy. For Ac-QQQQQQSSSQQQQ-NH_2, visible aggregates formed in 6 M GdnHCl within minutes after pH adjustment. Subsequent chromatography, under the same conditions as for Ac-NNNNNSSSNNNN-NH_2, revealed that less than 50% of the Ac-QQQQQQSSSQQQQ-NH_2 remained soluble in 6 M GdnHCl.

Preparation of HET-s$_{218-289}$ Fibrils. For comparison with Ure2p$_{1-89}$, uniformly ^{15}N,^{13}C-labeled HET-s$_{218-289}$ (residues 218−289 of the *P. anserina* HET-s protein, with an additional C-terminal His_6 tag) was expressed in *E. coli*, using a protocol similar to that used for U-^{15}N,^{13}C-Ure2p$_{1-89}$. Inclusion bodies containing U-^{15}N,^{13}C-HET-s$_{218-289}$ were dissolved in 8 M GdnHCl, 150 mM NaCl, 0.1 M Tris, pH 8.0 and purified on a Talon nickel column. Purified protein was then desalted on a PD10 column at low pH, neutralized by addition of Tris, and allowed to form fibrils at 4 C for 5 days. The resulting gel-like solution was pelleted, washed 4× with deionized water, and lyophilized. Additional details are given in Supporting Information.

Electron Microscopy. Transmission electron microscope (TEM) images of Ure2p$_{1-89}$, Ac-NNNNNNSSSNNNN-NH_2, and Ac-QQQQQQSSSQQQQ-NH_2 fibrils or aggregates were obtained on FEI CM120 and Morgagni microscopes, operated at 120 kV and 80 kV, respectively. For negative staining, the samples were adsorbed onto freshly glow-discharged carbon-coated grids or carbon films supported on lacey carbon-coated grids for 150 s, rinsed twice with water, stained with 1% or 3% uranyl acetate for 100 s, blotted, and allowed to dry in air.

Solid-State NMR. NMR measurements were carried out at room temperature in a 14.1 T magnetic field (150.7 MHz ^{13}C NMR frequency; 60.7 MHz ^{15}N NMR frequency) using Varian Infinity and InfinityPlus spectrometers and a Varian 3.2 mm magic-angle spinning (MAS) NMR probe. Val-^{13}CO-Ure2p$_{1-89}$, Leu-^{13}CO-Ure2p$_{1-89}$, and Ala-$^{13}CH_3$-Ure2p$_{1-89}$ fibrils were lyophilized before packing into MAS rotors. Sample masses were 1.2, 4.0 mg, and 6.0 mg, respectively. Measurements of intermolecular ^{13}C−^{13}C dipole−dipole couplings were performed with the constant-time finite-pulse radiofrequency-driven recoupling (fpRFDR-CT) technique (*56*) that has been applied in previous studies of fibrils formed by several different peptides and proteins (*25*, *26*, *28*, *52*). As in previous studies, fpRFDR-CT data were acquired at an MAS frequency of 20.0 kHz with 15.0 μs ^{13}C π pulses, 5.0 μs ^{13}C $\pi/2$ pulses, a total ^{13}C−^{13}C recoupling period of 76.8 ms, and proton decoupling with a 110 kHz radiofrequency (rf) field. Pulsed spin-lock detection (*57*) was used to enhance sensitivity in fpRFDR-CT measurements on Val-^{13}CO-Ure2p$_{1-89}$ and Leu-^{13}CO-Ure2p$_{1-89}$ fibrils, but not Ala-$^{13}CH_3$-Ure2p$_{1-89}$ fibrils. Total fpRFDR-CT measurement times were 18 h for each sample, with a 4 s recycle delay. Although previous fpRFDR-CT measurements were carried out at 9.4 T, numerical simulations indicate that the 14.1 T field in the current measurements does not affect the results significantly. Simulations discussed below include the carbonyl ^{13}C chemical shift anisotropy (CSA) at 14.1 T.

2D ^{13}C−^{13}C NMR spectra of U-^{15}N,^{13}C-Ure2p$_{1-89}$ fibrils were acquired at an MAS frequency of 12.0 kHz, using finite-pulse radiofrequency-driven recoupling (fpRFDR) (*32*, *58*) with 25.0 μs ^{13}C π pulses and 110 kHz proton decoupling during the mixing period of 2.667 ms (i.e., 32 rotor periods). The ^{13}C carrier frequency was placed at 71.5 ppm. Identical conditions were used for 2D ^{13}C−^{13}C NMR spectra of β-amyloid and amylin fibrils discussed below. Spectra of U-^{15}N,^{13}C-Ure2p$_{1-89}$ fibrils were obtained in three conditions: (1) fully hydrated, pelleted fibrils from the initial fibrillization buffer, contained in a thin-walled 3.2 mm MAS rotor with a 36 μL sample volume; (2) lyophilized fibrils, contained in a thick-walled 3.2 mm MAS rotor with an 11 μL sample volume; (3) lyophilized fibrils in the thick-walled rotor, rehydrated by addition of 3 μL of deionized H_2O to the rotor. Linewidths, chemical shifts, and cross peak volumes in 2D spectra of pelleted fibrils and rehydrated fibrils were indistinguishable. 2D spectra of rehydrated fibrils (1.3 mg protein mass) are analyzed below because of their higher signal-to-noise ratio. Spectra of dry lyophilized fibrils showed significantly broader NMR lines than those of pelleted and rehydrated fibrils, as discussed below.

2D ^{15}N−^{13}C NMR spectra of U-^{15}N,^{13}C-Ure2p$_{1-89}$ fibrils were acquired at an MAS frequency of 12.0 kHz, using a 1.5 ms cross-polarization period between the t_1 and t_2 periods, with ^{15}N and ^{13}C rf fields optimized for one-bond ^{15}N−$^{13}C_\alpha$ polarization transfers.

For comparison, 2D ^{13}C−^{13}C and ^{15}N−^{13}C NMR spectra of U-^{15}N,^{13}C-HET-s$_{218-289}$ were obtained under nearly identical conditions. Lyophilized U-^{15}N,^{13}C-HET-s$_{218-289}$ fibrils (21 mg) were packed in a thin-walled 3.2 mm MAS rotor and rehydrated by addition of 15 μL of deionized water. After rehydration, spectra with linewidths similar to those reported previously for fully hydrated (pelleted, but never lyophilized) samples (*42*, *50*, *51*) were obtained.

^{13}C NMR chemical shifts reported below are relative to tetramethylsilane, based on an external L-alanine powder carboxylate signal at 177.95 ppm. ^{15}N NMR chemical shifts are relative to liquid NH_3, based on a calculated ratio of 0.4029075 between liquid NH_3 and L-alanine carboxylate NMR frequencies (*59*). 2D NMR data were processed with NMRPipe software (*60*). Cross peak volumes were extracted from 2D ^{13}C−^{13}C NMR spectra with ImageJ software (available at http://rsb.info.nih.gov/ij/), after converting the 2D spectra from NMRPipe format to grayscale TIFF format. Note that conversion to TIFF format did not entail any distortion or loss of precision in the NMR signal amplitudes.

RESULTS

Fibril Formation Verified by Electron Microscopy. Figure 1 shows TEM images of Ure2p$_{1-89}$ fibrils prepared as described above. Fibrils are 6−25 nm in width, and appear to be composed of finer filaments with 3−6 nm widths. Images in Figure 1 are similar to previously reported images of Ure2p$_{1-89}$ fibrils and fibrils formed by shorter segments of the Ure2p prion domain (*1*, *16*), including *in vitro*

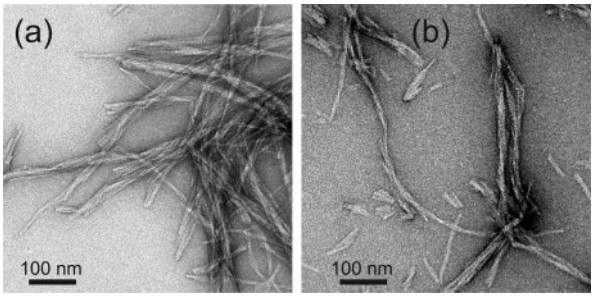

FIGURE 1: TEM images of Ure2p$_{1-89}$ fibrils, negatively stained with uranyl acetate. Samples are ^{13}C-labeled at Leu carbonyl sites (a) or uniformly ^{15}N,^{13}C-labeled (b).

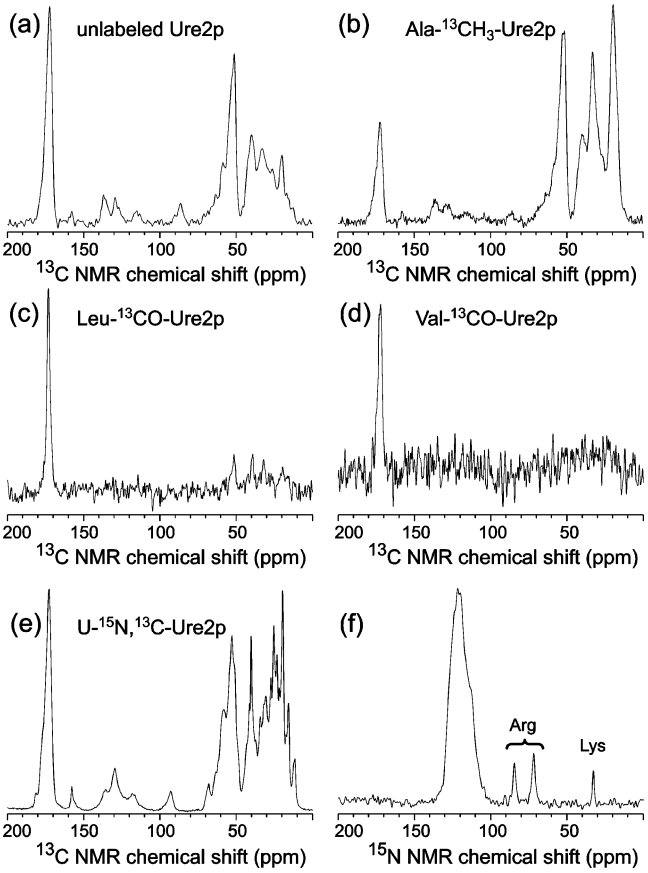

FIGURE 2: Solid state ^{13}C NMR (a−e) and ^{15}N NMR (f) spectra of Ure2p$_{1-89}$ fibrils. Fibrils were not isotopically labeled (a), ^{13}C-labeled at side chain methyl carbons of Ala residues (b), or ^{13}C-labeled at backbone carbonyl sites of Leu residues (c) or Val residues (d), and were lyophilized. Uniformly ^{15}N,^{13}C-labeled fibrils (e, f) were fully hydrated. Signals arising from side chains of Arg and Lys residues are indicated in part d. All spectra were acquired in a 14.1 T magnetic field with MAS at 13.00 kHz (a, b), 20.00 kHz (c, d), or 12.00 kHz (e, f). Spectra were obtained in 5000, 4096, 156, 136, 6144, and 1696 scans (a−f, respectively).

Ure2p$_{1-89}$ fibrils that were found to be capable of inducing [URE3] in *S. cerevisiae* (*8*).

Parallel β-Sheets Indicated by Intermolecular $^{13}C-^{13}C$ Dipole−Dipole Couplings. Figure 2 shows 1D ^{13}C and ^{15}N NMR spectra of the Ure2p$_{1-89}$ fibrils. The spectrum of an unlabeled sample is shown in Figure 2a. The spectrum of the Ala-$^{13}CH_3$-Ure2p$_{1-89}$ sample (Figure 2b) shows an enhanced methyl carbon line at 20 ppm. Other aliphatic carbon signals (25−70 ppm) are also enhanced relative to the carbonyl line (172 ppm). Assuming that the carbonyl line arises from natural-abundance ^{13}C nuclei (1.1% abundance), analysis of peak areas in Figures 2a and 2b indicates that C_α sites in Ala-$^{13}CH_3$-Ure2p$_{1-89}$ (48−60 ppm) have an average ^{13}C content of approximately 2.7% and methyl sites (15−25 ppm) have an average ^{13}C content of approximately 7.3%. Assuming that Ala methyl sites are 100% ^{13}C-enriched, the 27 methyl sites of other residues have an average ^{13}C content of approximately 3.7%. Thus, Figure 2b is consistent with a high level of enrichment of Ala methyl sites and much lower enrichment (through scrambling of the labeled alanine in the culture medium) of other aliphatic sites.

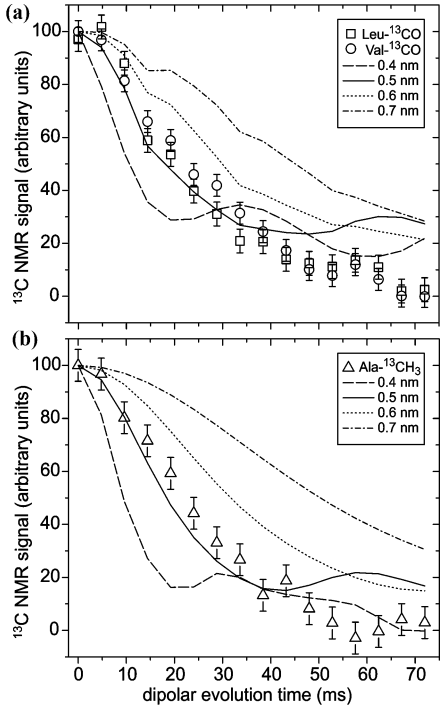

FIGURE 3: Measurements of intermolecular $^{13}C-^{13}C$ dipole−dipole couplings, which depend on intermolecular distances, in Ure2p$_{1-89}$ fibrils using the fpRFDR-CT technique. Signal contributions from natural-abundance ^{13}C are subtracted as described in the text. Simulated curves are for linear chains of ^{13}C nuclei with the indicated nearest-neighbor internuclear distances. (a) Data for fibrils that were ^{13}C-labeled at backbone carbonyl sites of Leu and Val residues. (b) Data for fibrils that were ^{13}C-labeled at methyl sites of Ala residues.

Figures 2c and 2d show 1D ^{13}C NMR spectra of Leu-^{13}CO-Ure2p$_{1-89}$ and Val-^{13}CO-Ure2p$_{1-89}$ fibrils. A single ^{13}C NMR line from the labeled sites is observed in each spectrum, centered at a chemical shift value (172.5 ppm for Val-^{13}CO-Ure2p$_{1-89}$, 173.0 ppm for Leu-^{13}CO-Ure2p$_{1-89}$) that is significantly upfield from reported random coil carbonyl chemical shifts (174.6 ppm for Val, 175.9 ppm for Leu) (*61*). An upfield shift for carbonyl sites is characteristic of β-strands (*25*, *27*, *32*, *33*, *52*, *62*), indicating that all labeled Val and Leu sites are located in β-sheets. The enhancement of carbonyl signals relative to aliphatic signals in Figures 2c and 2d is consistent with the high level of ^{13}C enrichment indicated by mass spectrometry (see above).

The spectrum in Figure 2c does not show a clear peak near 20 ppm that would arise from ^{13}C labels at side chain methyl sites of alanine residues, consistent with the low incorporation of Ala-$^{13}CH_3$ in the Leu-^{13}CO-Ure2p$_{1-89}$ sample (see Materials and Methods).

Figure 3 shows fpRFDR-CT data for Val-^{13}CO-Ure2p$_{1-89}$, Leu-^{13}CO-Ure2p$_{1-89}$, and Ala-$^{13}CH_3$-Ure2p$_{1-89}$ fibrils. The

fpRFDR-CT technique (*25*, *26*, *28*, *52*, *56*) is a measurement of magnetic dipole−dipole couplings among ^{13}C nuclei, which are proportional to the inverse cube of the internuclear distances. More rapid decay of the fpRFDR-CT signal therefore indicates shorter internuclear distances. Numerical simulations for ideal linear chains of ^{13}C nuclei with various nearest-neighbor spacings are included in Figure 3 for comparison with the experimental data. The simulations include five ^{13}C nuclei, powder averaging, and the full time dependence of rf fields and $^{13}C-^{13}C$ dipole−dipole interactions during fpRFDR-CT measurements. Simulations in Figure 3a additionally include carbonyl CSA interactions, assuming a CSA tensor orientation and principal values (70 ppm, 10 ppm, and −80 ppm, relative to the rf carrier frequency) appropriate for backbone carbonyl sites (*63*). To minimize "end effects" in these simulations, spin polarization was placed only on the central ^{13}C nucleus initially, and NMR signals from all spins were detected subsequently. Contributions of natural-abundance ^{13}C nuclei to the experimental fpRFDR-CT data were subtracted before plotting the data in Figure 3. Natural-abundance corrections in Figure 3a assume 1.5 natural-abundance carbonyl or carboxylate ^{13}C nuclei per $Ure2p_{1-89}$ molecule (based on the amino acid sequence, and representing 33.3% of the total signal in Leu-^{13}CO-$Ure2p_{1-89}$ data and 27.3% of the total signal in Val-^{13}CO-$Ure2p_{1-89}$ data) and a linear decay of the natural-abundance signal to 70% of its initial value at the maximum dipolar evolution time (based on earlier measurements on unlabeled Sup35NM fibrils (*25*)). Corrections in Figure 3b assume that 50% of the methyl ^{13}C NMR signal in Ala-$^{13}CH_3$-$Ure2p_{1-89}$ arises from methyl carbons at residues other than alanine, based on the analysis of isotopic enrichment and scrambling described above. Uncorrected data for all three samples are shown in Supporting Information.

Experimental fpRFDR-CT signals for all three fibril samples decay to approximately 30% of their initial values in 35 ms, indicating internuclear distances of 0.50 ± 0.04 nm. Given the distribution of Val and Leu residues in $Ure2p_{1-89}$, at residues 9, 12, 16, 19, 43, 58, and 81, and the β-strand backbone conformation at these residues indicated by the ^{13}C chemical shifts, the 0.50 ± 0.04 nm internuclear distances are assigned to intermolecular distances between like residues in parallel β-sheets. Based solely on data from the Val-^{13}CO-$Ure2p_{1-89}$ and Leu-^{13}CO-$Ure2p_{1-89}$ samples (Figure 3a), these parallel β-sheets could have in-register alignment (i.e., intermolecular backbone hydrogen bonding of the backbone amide and carbonyl groups of residue k in one β-strand to the carbonyl group of residue $k - 1$ and the amide group of residue $k + 1$ of a neighboring β-strand in the same β-sheet), which would lead to internuclear distances of 0.48 ± 0.01 nm. Alternatively, the parallel β-sheets could have a one-residue shift of the intermolecular alignment, which would result in nearest-neighbor intermolecular distances of approximately 0.53 nm for backbone carbonyl labels, as can be seen by examination of parallel β-sheets in amyloid fibril models (*41*, *64*) or β-sheet crystal structures (*48*). As in earlier studies of $Ure2p_{10-39}$ fibrils, Sup35NM fibrils, and full-length β-amyloid fibrils (*25*, *26*, *28*, *52*), a one-residue shift of the intermolecular alignment is ruled out by the fpRFDR-CT data for Ala-$^{13}CH_3$-$Ure2p_{1-89}$ fibrils (Figure 3b), because nearest-neighbor intermolecular distances between alanine methyl carbons would exceed 0.65 nm in any out-of-register β-sheet structure. Thus, the fpRFDR-CT data in Figure 3 imply an in-register parallel β-sheet structure in $Ure2p_{1-89}$ fibrils.

Spectra in Figures 2a−2d and fpRFDR-CT data in Figure 3 were obtained from dry, lyophilized samples. Therefore, we expect these spectra and data to be unaffected by the molecular motions that affect 2D spectra of hydrated samples, which are discussed below. All labeled Leu and Val residues are expected to contribute with approximately equal intensities in Figures 2 and 3. This interpretation is supported by earlier investigations of effects of hydration on similar data for Sup35NM fibrils (*25*).

At dipolar evolution times beyond 45 ms, experimental data in Figure 3 deviate significantly from the simulated data for 0.5 nm internuclear distances. We attribute these deviations to effects of transverse nuclear spin relaxation on the experimental data. In earlier simulations of fpRFDR-CT data for two-spin systems (*28*), transverse nuclear spin relaxation was shown to produce a damping of oscillations at long evolution times, similar to the effects in Figure 3. Inclusion of transverse nuclear spin relaxation in simulations for the five-spin systems considered in Figure 3 was not feasible from the standpoint of computation time.

Solid-State NMR of Uniformly Labeled $Ure2p_{1-89}$ Fibrils. Figures 2e and 2f show 1D ^{13}C and ^{15}N NMR spectra of U-^{15}N,^{13}C-$Ure2p_{1-89}$ fibrils in hydrated form. 2D $^{15}N-^{13}C$ and $^{13}C-^{13}C$ NMR spectra, obtained with conditions described above, are shown in Figures 4 and 5. One motivation for our experiments on U-^{15}N,^{13}C-$Ure2p_{1-89}$ fibrils was to determine whether their NMR spectra are as well-resolved as spectra of uniformly labeled HET-$s_{218-289}$ fibrils obtained by Siemer et al. (*50*, *51*) The spectra in Figures 2, 4, and 5 show that this is not the case. Whereas ^{13}C NMR linewidths less than 0.5 ppm were observed in hydrated HET-$s_{218-289}$ fibrils, and many individual cross peaks were resolved in 2D spectra of hydrated HET-$s_{218-289}$ fibrils, linewidths in spectra of hydrated U-^{15}N,^{13}C-$Ure2p_{1-89}$ fibrils (Figures 2c, 2d, 4a, 4b, 4c, and 5) are generally larger by factors of three or more, and few individual cross peaks are resolved in the 2D spectra. In Figure 5, intraresidue cross peaks between backbone ^{15}N and $^{13}C_\alpha$ lines merge into a single, broad cross peak. In Figure 4c, most $^{13}C-^{13}C$ cross peaks merge into broad features with no structure attributable to individual residues. In the lyophilized state (Figures 4e and 4f), $^{13}C-^{13}C$ cross peaks are even broader and more poorly resolved. No changes in ^{13}C chemical shifts are observed that might indicate major structural changes upon lyophilization, consistent with the observation that solid-state NMR spectra of pelleted and rehydrated (see Materials and Methods) $Ure2p_{1-89}$ fibrils are indistinguishable.

Figure 6 shows our own 2D $^{13}C-^{13}C$ and $^{15}N-^{13}C$ spectra of U-^{15}N,^{13}C-HET-$s_{218-289}$ fibrils, obtained under essentially the same experimental conditions as the spectra in Figures 4 and 5. Spectra in Figure 6 are in good agreement with the results of Siemer et al. (*50*, *51*). Although HET-$s_{218-289}$ and $Ure2p_{1-89}$ have similar molecular weights, 2D spectra of U-^{15}N,^{13}C-HET-$s_{218-289}$ fibrils are much better resolved. Typical ^{13}C and ^{15}N NMR linewidths for backbone sites are 0.7 and 1.0 ppm, respectively. It is worth noting that the spectra in Figure 6 were obtained from a sample that was lyophilized and subsequently rehydrated by addition of water into the MAS rotor. NMR linewidths and chemical shifts in

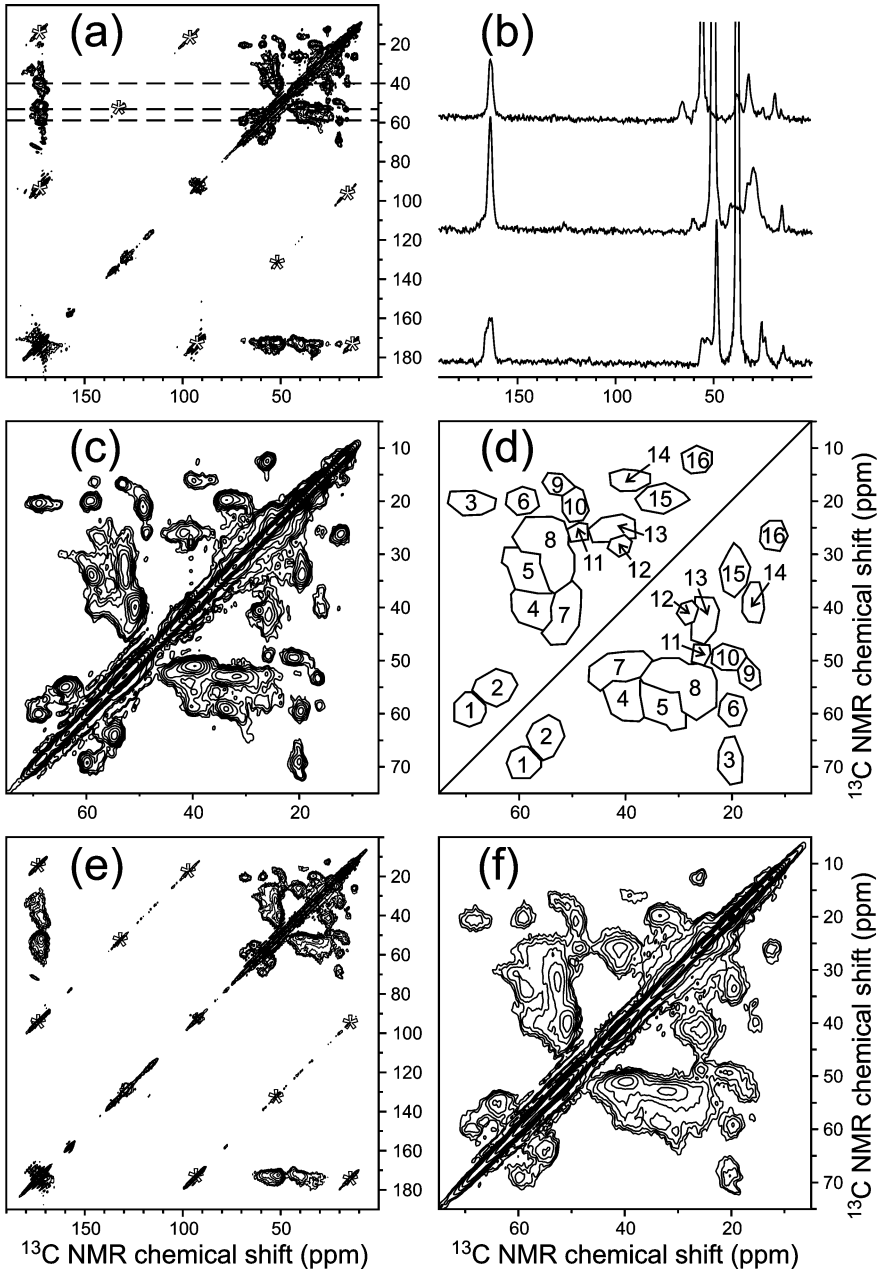

FIGURE 4: 2D ^{13}C−^{13}C NMR spectra of U-^{15}N,^{13}C-Ure2p$_{1-89}$ fibrils. (a) Full spectrum of hydrated fibrils. Asterisks indicate cross peaks among spinning sidebands. (b) 1D slices at positions indicated by dashed lines in part a, to illustrate the signal-to-noise ratio of cross peaks in the 2D spectra. (c) Aliphatic region of the spectrum in part a. (d) Cross peak regions for which signal volumes are analyzed as described in the text. Signal volumes and assignments to one-bond and two-bond cross peaks of specific sets of amino acids are given in Table 1. (e, f) Full and aliphatic regions of the 2D spectrum of dry, lyophilized fibrils. The number of scans per complex t_1 point was 1544 (parts a and c) or 2816 (parts e and f), with a 19.2 μs t_1 increment and 150 points. Contour levels in all spectra increase by successive factors of 1.5.

Figure 6 are indistinguishable from those observed in 2D spectra of hydrated U-^{15}N,^{13}C-HET-s$_{218-289}$ prior to lyophilization. Data in Figure 6 show that the relatively low resolution in 2D spectra of U-^{15}N,^{13}C-Ure2p$_{1-89}$ fibrils is not a consequence of our sample preparation or NMR measurement conditions, but instead is a consequence of the inherent properties of Ure2p$_{1-89}$ fibrils.

The signals in Figure 4c occur in regions that can be assigned to one-bond and two-bond cross peaks of groups of residues, based on the known ^{13}C chemical shift ranges for each residue (*61*). Regions whose total cross peak volumes can be determined from the experimental spectrum are shown in Figure 4d. The corresponding assignments and measured volumes are given in Table 1. Note that the single Ala residue in Ure2p$_{1-89}$ contributes cross peak signals assignable to both β-strand and non-β-strand conformations (regions 10 and 9, respectively). This observation suggests that our Ure2p$_{1-89}$ fibrils are polymorphic at the molecular structural level, as previously observed for other amyloid fibrils (*12*, *52*, *65*, *66*). Molecular-level structural variations in Ure2p fibrils *in vivo* may give rise to [URE3] strains.

The Ure2p$_{1-89}$ sequence contains 33 Asn, 10 Gln, and 10 Ser residues. If all one-bond cross peaks had equal intensities, one might expect the signals from Asn, Gln, and Ser residues to dominate the spectrum in Figure 4c. A cursory examination of this spectrum and of Table 1 suggests that Asn, Gln, and Ser signals might be anomalously weak, but a definite conclusion cannot be drawn without calibration of the

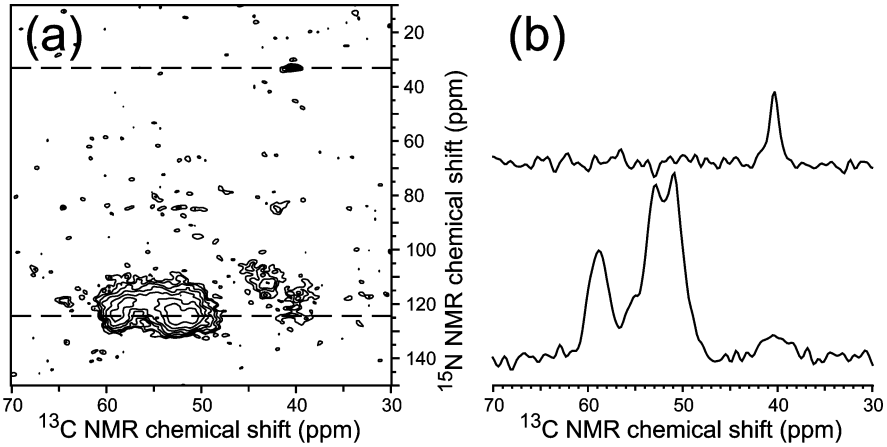

FIGURE 5: (a) 2D ^{15}N−^{13}C NMR spectrum of U-^{15}N,^{13}C-Ure2p$_{1-89}$ fibrils in the hydrated state. The number of scans per complex t_1 point was 272, with a 100.0 μs t_1 increment and 64 points. (b) 1D slices at positions indicated by dashed lines in part a.

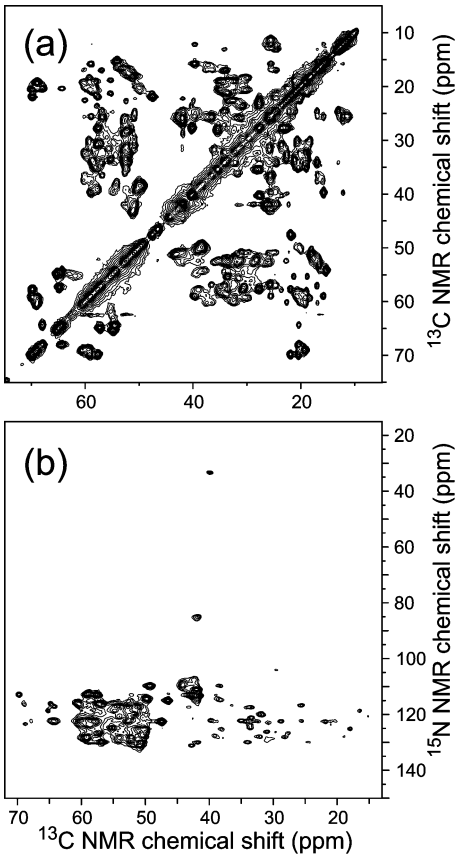

FIGURE 6: 2D solid-state NMR spectra of U-^{15}N,^{13}C-HET-s$_{218-289}$ fibrils, for comparison with the spectra of U-^{15}N,^{13}C-Ure2p$_{1-89}$ fibrils in Figures 4 and 5. (a) 2D ^{13}C−^{13}C NMR spectrum obtained with a 2.56 ms mixing period, 12.50 kHz MAS frequency, 96 scans per complex t_1 point, 21.0 μs t_1 increment, and 480 points. (b) 2D ^{15}N−^{13}C NMR spectrum obtained with a 4.0 ms ^{15}N−^{13}C cross-polarization period, 12.50 kHz MAS frequency, 128 scans per complex t_1 point, 105.0 μs t_1 increment, and 150 points.

intrinsic cross peak volumes for individual residues under our experimental conditions. Therefore, we measured one-bond and two-bond cross peak volumes in 2D ^{13}C−^{13}C spectra of amyloid fibrils formed by several peptides that had been synthesized with uniformly labeled residues at selected sites for independent structural studies, including the 40-residue β-amyloid peptide (Aβ_{1-40}), residues 11−25 of the β-amyloid peptide (Aβ_{11-25}) and the 37-residue amylin peptide. 2D spectra of these samples are shown in Figure 7.

Table 1: Relative Cross Peak Volumes in the Experimental Two-Dimensional ^{13}C−^{13}C NMR Spectrum of U-^{15}N,^{13}C-Ure2p$_{1-89}$ Fibrils Shown in Figure 4c

cross peak region[a]	assignment[b]	fraction of total cross peak volumes[c]
1	5T$_{\alpha\beta}$	0.0416
2	10S$_{\alpha\beta}$	0.0752
3	5T$_{\beta\gamma}$	0.0343
4	3I$_{\alpha\beta}$, 2F$_{\alpha\beta}$	0.0890
5	4V$_{\alpha\beta}$	0.0668
6	4V$_{\alpha\gamma}$, 3I$_{\alpha\gamma2}$, 5T$_{\alpha\gamma}$	0.0263
7	33N$_{\alpha\beta}$, 3L$_{\alpha\beta}$, 2D$_{\alpha\beta}$	0.2022
8	2M$_{\alpha\beta}$, 2M$_{\alpha\gamma}$, 10Q$_{\alpha\beta}$, 10Q$_{\alpha\gamma}$, 1K$_{\alpha\beta}$, 1K$_{\alpha\gamma}$, 4R$_{\alpha\beta}$, 4R$_{\alpha\gamma}$, 3I$_{\alpha\gamma1}$, 3E$_{\alpha\beta}$, 3E$_{\alpha\gamma}$, 1H$_{\alpha\beta}$	0.2028
9	1A$_{\alpha\beta}$ (non-β-strand)	0.0142
10	1A$_{\alpha\beta}$ (β-strand)	0.0345
11	uncertain	0.0097
12	1K$_{\delta\epsilon}$	0.0185
13	3I$_{\beta\gamma1}$, 4R$_{\gamma\delta}$, 3L$_{\beta\gamma}$	0.0598
14	3I$_{\beta\gamma2}$	0.0240
15	4V$_{\beta\gamma}$	0.0744
16	3I$_{\gamma1\delta}$	0.0267

[a] Numbering corresponds to Figure 4d. [b] Numbers preceding one-letter amino acid codes are the number of copies of each amino acid in the Ure2p$_{1-89}$ sequence. Subscripts indicate carbon sites whose NMR signals are connected by the cross peak. [c] Includes cross peaks on both sides of the diagonal in Figure 4d.

Table 2 contains the intrinsic cross peak volumes for residues that are present in Ure2p$_{1-89}$, determined or estimated from the spectra in Figure 7.

Cross peak volumes in Table 2 are normalized to the volumes of cross peaks between α-carbon and β-carbon signals of Ala and Ser residues, because all samples in Figure 7 contain either a uniformly labeled Ala or a uniformly labeled Ser residue. The equivalence of A$_{\alpha\beta}$ and S$_{\alpha\beta}$ cross peak volumes is supported by the near equality of the ratios of V$_{\alpha\beta}$ to A$_{\alpha\beta}$ and V$_{\alpha\beta}$ to S$_{\alpha\beta}$ volumes in the experimental spectra, as well as the near equality of the ratios of G$_{CO\alpha}$ to A$_{\alpha\beta}$ and G$_{CO\alpha}$ to S$_{\alpha\beta}$ volumes. In addition, since both Ala and Ser residues are three-spin ^{13}C systems, one expects similar cross peak volumes from basic principles of nuclear spin dynamics under the fpRFDR pulse sequence used to obtain the experimental 2D ^{13}C−^{13}C spectra.

Given the amino-acid-specific cross peak volumes in Table 2 and the volumes for U-^{15}N,^{13}C-Ure2p$_{1-89}$ fibrils in Table

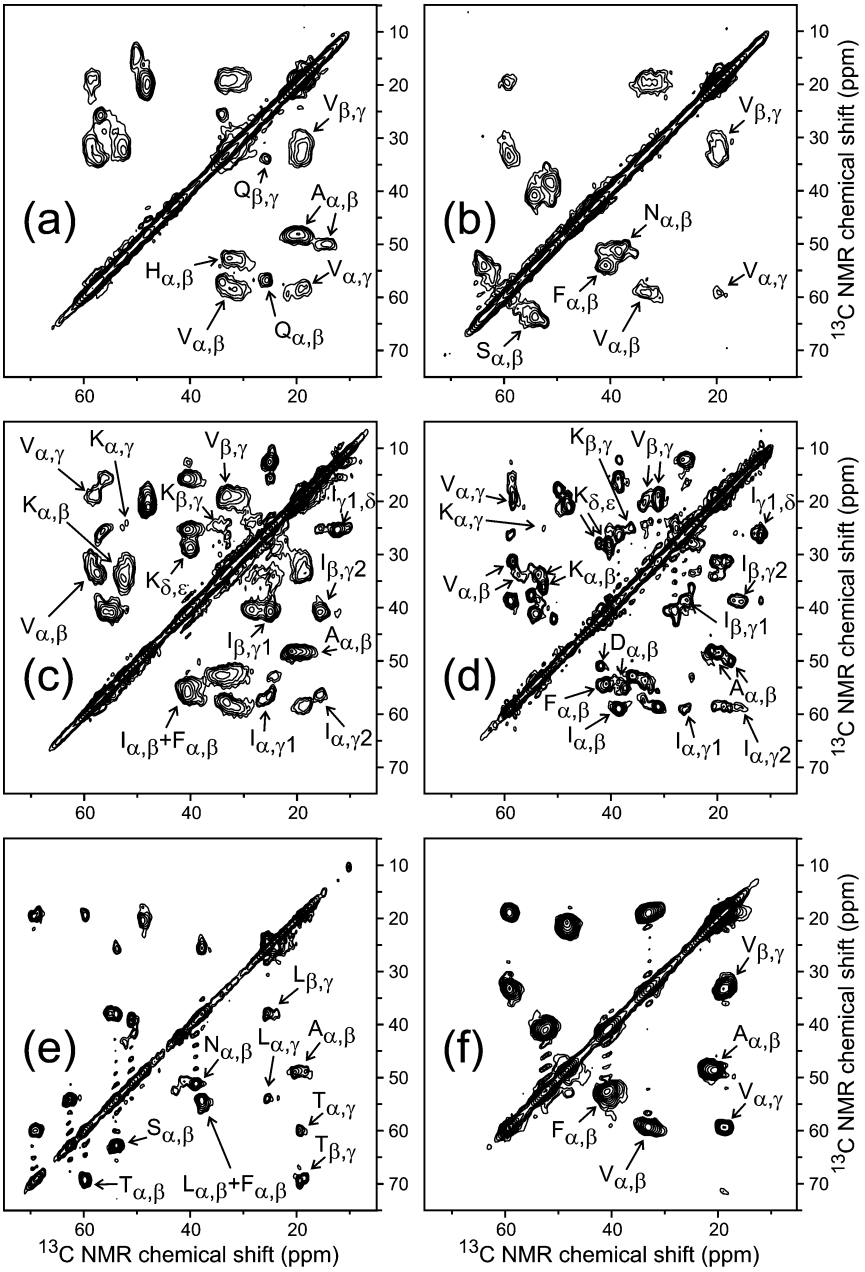

FIGURE 7: 2D ^{13}C−^{13}C NMR spectra of various amyloid fibril samples, used to determine the amino-acid-specific intrinsic cross peak volumes in Table 2. (a) Aβ_{1-40} fibrils with uniform ^{15}N and ^{13}C labeling of H14, Q15, A21, V36, and G37. (b) Aβ_{1-40} fibrils with uniform ^{15}N and ^{13}C labeling of F20, S26, N27, G33, G38, and V39. (c) Aβ_{1-40} fibrils with uniform ^{15}N and ^{13}C labeling of K16, F19, A21, E22, I32, and V36. (d) Aβ_{1-40} fibrils with uniform ^{15}N and ^{13}C labeling of F20, D23, V24, K28, G29, A30, and I31. (e) Amylin fibrils with uniform ^{15}N and ^{13}C labeling of A8, S19, F23, G24, L27, N35, and T36. (f) Aβ_{11-25} fibrils with uniform ^{15}N and ^{13}C labeling of V18, F19, F20, and A21. Experimental conditions for all spectra were identical to those in Figure 4 except that the number of scans per t_1 point varied with sample quantities. Samples in parts d and e were rehydrated after lyophilization. Other samples were lyophilized but not hydrated.

1, signals from Asn and Ser residues are indeed weaker than expected if the entire Ure2p$_{1-89}$ sequence were contributing fully to the spectrum in Figure 4c. One possible interpretation of this observation is that, in the fibrillar state, Ure2p$_{1-89}$ contains disordered, non-β-strand segments between the β-strand segments that comprise the ordered, parallel cross-β structure. Motions of the disordered segments would strongly attenuate their contributions to 2D ^{13}C−^{13}C spectra by producing relatively short T_2 and $T_{1\rho}$ spin relaxation times, by interfering with MAS and proton decoupling, or by averaging out ^{13}C−^{13}C dipole−dipole couplings. This interpretation is suggested by NMR studies of HET-s$_{218-289}$ and α-synuclein fibrils (*42*, *50*, *51*, *66*, *67*), which revealed the presence of both rigid, β-sheet-forming segments (observable in solid-state NMR spectra) and mobile "tail" and "loop" segments (not observable in solid-state NMR spectra). Consequently, we attempted to fit the cross peak volumes in Table 1 with a simple model in which the observed signals arise from n segments of the Ure2p$_{1-89}$ sequence, each with a minimum length of eight residues, separated by invisible segments with a minimum length of three residues. A computer program was written to exhaustively search all locations and lengths of the n segments and calculate the total squared deviation Δ^2 between experimental cross peak volumes E_i (from Table 1) and calculated volumes C_i (using Table 2), with $\Delta^2 \equiv \sum_i[(E_i/E_T) - (C_i/C_T)]^2/(C_i/C_T)^2$, $E_T \equiv \sum_i E_i$, and $C_T \equiv \sum_i C_i$. With this definition of Δ^2, deviations for each cross peak region i are weighted inversely by the

Table 2: Amino-Acid-Specific, Intrinsic Cross Peak Volumes Used in the Analysis of the Two-Dimensional $^{13}C-^{13}C$ NMR Spectrum of U-^{15}N,^{13}C-Ure2p$_{1-89}$ Fibrils[a]

	cross peak				
amino acid (X)	$X_{\alpha\beta}$	$X_{\beta\gamma}$	$X_{\alpha\gamma}$	$X_{\delta\epsilon}$	$X_{\gamma\delta}$
A	1.00				
S	1.00				
V	0.56 ± 0.05	0.80 ± 0.06	0.25 ± 0.05		
F	0.48 ± 0.06				
I	0.48	0.40 ± 0.08,[b] 0.36 ± 0.02[c]	0.18 ± 0.06,[b] 0.14 ±0.02[c]		0.46 ± 0.01[b]
Q	0.37		0.08[d]		
H	0.35				
N	0.87 ± 0.05				
K	0.66	0.16 ±0.06	0.08 ± 0.02	0.44 ± 0.06	
E	0.31		0.08[b]		
T	0.61	0.61	0.21		
L	0.35	0.41	0.15		
D	0.40				
R	0.50[d]		0.08[d]		0.44[d]
M	0.50[d]		0.08[d]		

[a] Except where indicated, all values are determined from experimental spectra in Figure 7. Error limits indicate the range of values for a given cross peak when more than one value could be extracted from the experimental spectra. All cross peak volumes are relative to $A_{\alpha\beta}$ and $S_{\alpha\beta}$ volumes, which are taken to be 1.00. [b] For $\gamma 1$ site. [c] For $\gamma 2$ site. [d] Estimated from corresponding values for L and K, but not determined directly from experimental spectra.

corresponding cross peak volumes, which is appropriate if the dominant source of error arises from uncertainty in the calibration of intrinsic cross peak volumes. In calculating Δ^2, cross peak regions 9 and 10 were combined and region 11 was ignored.

Figure 8 summarizes the output of this program. The best fits to the experimental cross peak volumes were achieved with $n = 4$. The minimum value of Δ^2, equal to 0.7132, corresponds to an average deviation of 23% between E_i/E_T and C_i/C_T values. All values of n greater than or less than four produced values of Δ^2 that exceeded 0.89.

Fibril Formation by Ac-NNNNNNSSSNNNN-NH$_2$ and Ac-QQQQQQSSSQQQQ-NH$_2$. The best-fit configurations of observable and invisible segments in Figure 8 place residues 45−57, with sequence NNNNNNSSSNNNN, in an invisible segment. This result is surprising in light of previous evidence that other Asn-rich proteins form amyloid fibrils (*25*, *26*, *68*) and that fibril structures may be stabilized by interactions among side chain amide groups of Asn residues (*48*, *69*). Additionally, crystal structures of β-helical proteins reveal the presence of "Asn ladders" that apparently stabilize the β-helical fold (*70*). We therefore investigated the propensity of the peptide Ac-NNNNNNSSSNNNN-NH$_2$ to form amyloid fibrils. Solutions of Ac-NNNNNNSSSNNNN-NH$_2$ in phosphate buffer were incubated at room temperature, without deliberate agitation. TEM images of resulting aggregates were recorded, as shown in Figure 9. At a peptide concentration of 35 μM, only amorphous aggregates were observed, and only at low densities on the electron microscope grids (Figure 9a). No fibrillar aggregates were observed, even after 120 days of incubation, suggesting that the equilibrium solubility of this peptide exceeds 35 μM. At concentrations of 140 μM and 560 μM, fibrillar aggregates were observed, with densities on the electron microscope grids that increased with peptide concentration (Figures 9b and 9c). In contrast, peptides such as Ure2p$_{10-39}$ (sequence SNLSNALRQVNIGNRNSNTTTDQSNINFEF) form fibrils within several minutes at concentrations below 50 μM (*26*). These observations suggest that β-sheet formation by residues 45−56 is not a driving force for fibrillization of Ure2p$_{1-89}$.

The analogous Gln-rich peptide Ac-QQQQQQSSSQQQQ-NH$_2$ was found to form fibrils rapidly even in 6 M GdnHCl (Figure 9d). Thus, although prior proposals and experimental evidence indicate that polar zipper interactions among side chain amide groups of either Gln or Asn residues can stabilize amyloid fibrils, it appears that Gln and Asn residues are not equivalent in this regard. We speculate that the shorter side chain of Asn may restrict the capacity of polyAsn segments to form networks of polar zipper interactions with optimal geometry in cross-β structures.

DISCUSSION

The principal conclusions to be drawn from the data presented above are as follows: (1) β-sheets in fibrils formed *in vitro* by the prion domain of Ure2p have an in-register parallel intermolecular alignment; (2) the parallel β-sheet structure includes all Leu and Val residues in Ure2p$_{1-89}$, implying that it spans residues 9−81; (3) the parallel β-sheet structure of Ure2p$_{1-89}$ may contain both rigid and mobile segments, leading to variations in solid-state NMR signal amplitudes from different segments; (4) residues 45−57, containing ten Asn residues, may be a relatively mobile and disordered segment; (5) the degree of structural order or structural homogeneity in Ure2p$_{1-89}$ fibrils is not as high as in HET-s$_{218-289}$ fibrils, suggesting that the high degree of molecular structural order in the HET-s prion of *P. anserina* is a consequence of special properties of HET-s.

Parallel β-sheets have now been observed in many amyloid fibrils (*23*−*26*, *28*−*30*, *48*, *52*, *71*−*74*), including fibrils formed by the prion domains of the [URE3] and [PSI] prions of *S. cerevisiae* as well as fibrils formed by the β-amyloid and amylin peptides associated with Alzheimer's disease and type 2 diabetes. To date, antiparallel β-sheets have only been found in fibrils formed by relatively short peptides that contain only one β-strand segment (*31*−*33*, *35*, *45*). Formation of parallel β-sheets with purely intermolecular hydrogen bonding of neighboring β-strands is most likely driven by favorable interactions among like residues, including hydrophobic interactions among hydrophobic groups and polar

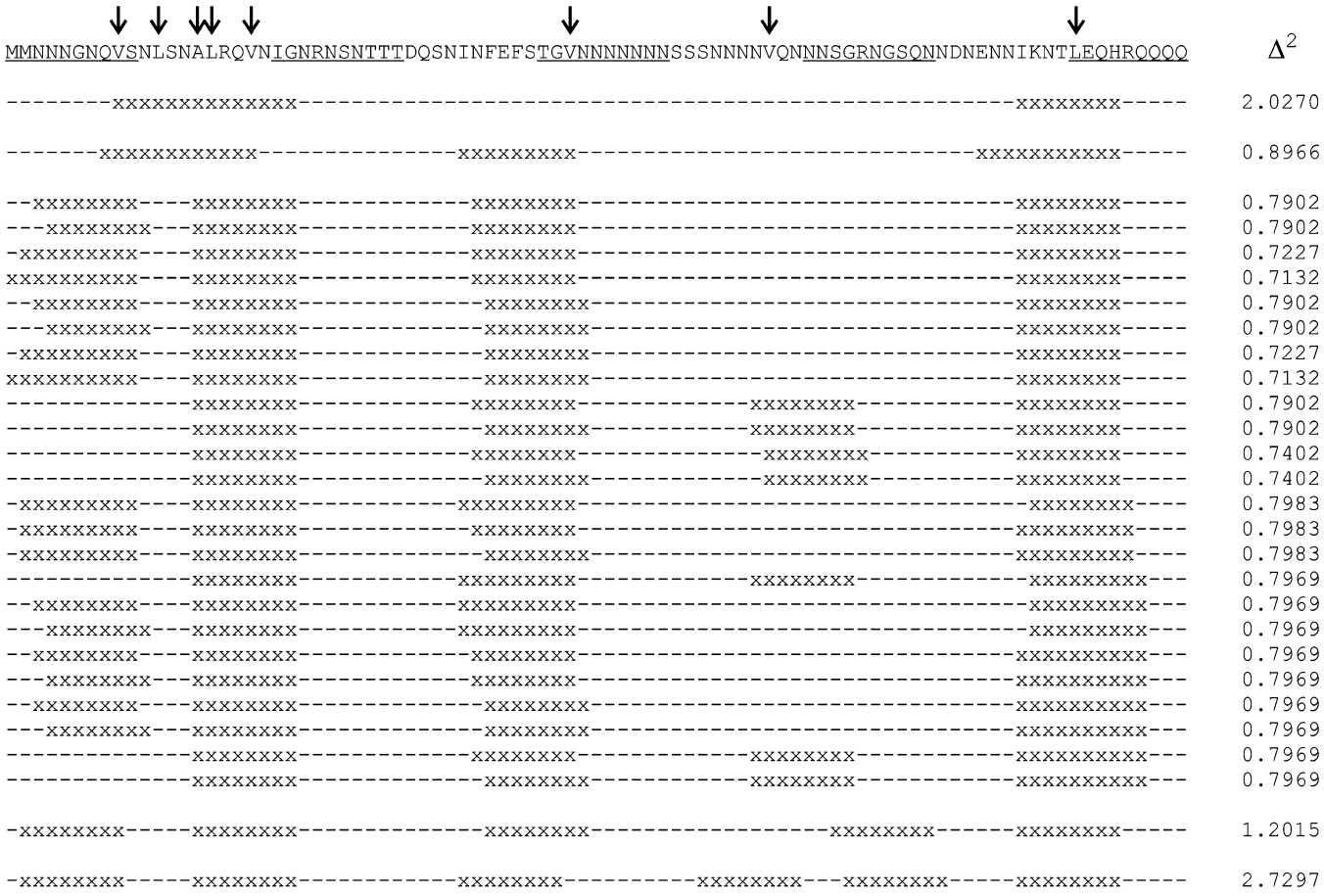

FIGURE 8: Results of fitting the experimental cross peak volumes in the 2D $^{13}C-^{13}C$ spectrum of U-^{15}N,^{13}C-Ure2p$_{1-89}$ fibrils, from Figure 4c and Table 1, with calculated cross peak volumes based on Table 2, assuming that the experimentally observed signals arise from a specified number of rigid segments of Ure2p$_{1-89}$ and that intervening segments are relatively mobile and therefore do not contribute to solid-state NMR signals. Residues in rigid and mobile segments are indicated by x and − symbols, respectively. The 24 configurations with lowest total squared deviation Δ^2, all of which contain four rigid segments, are shown along with the best-fit configurations that contain two, three, five, and six rigid segments. (Arrows above the amino acid sequence indicate the Val, Leu, and Ala sites that were ^{13}CO- or $^{13}CH_3$-labeled for fpRFDR-CT measurements reported in Figure 3. The sequence is underlined in groups of ten residues to facilitate identification of residue numbers. His-tag is omitted.)

zipper interactions (*26*, *47*, *48*) among side chains of Gln, Asn, and possibly other polar, uncharged residues.

Residues 9−81 of Ure2p$_{1-89}$ cannot form a single β-strand, because the length of this β-strand (approximately 25 nm) would exceed the widths of Ure2p$_{1-89}$ fibrils observed in TEM images. Alternation of β-strand segments with "bend" or "loop" segments, as demonstrated (*41*−*44*, *74*) or suggested (*25*, *66*, *71*, *73*, *75*, *76*) for other amyloid fibril structures, is a strong possibility. The anomalous cross peak volumes in 2D solid-state NMR spectra presented above suggest that certain non-β-strand segments may be relatively mobile, thereby attenuating their solid-state NMR signals. The amplitudes and time scales of motion cannot be determined from the present data, because several mechanisms of signal attenuation that operate in different motional regimes are possible. Surprisingly, after calibration of the amino-acid-specific, intrinsic cross peak volumes as explained above, the best fits to 2D $^{13}C-^{13}C$ NMR cross peak volumes for Ure2p$_{1-89}$ place residues 45−56 in a mobile segment. The fact that the corresponding peptide Ac-NNNNNNSSSNNNN-NH_2 does not aggregate readily at 35 μM concentration (whereas the analogous Gln-rich peptide aggregates quickly in 6 M GdnHCl) supports the possibility that intermolecular interactions involving this segment are not an important stabilizing factor for Ure2p$_{1-89}$ fibrils. Ross et al. have shown that Ure2p mutants with scrambled prion domain sequences are capable of acting as prions even when the prion domain contains no more than three sequential Asn residues (*49*).

Solid-state NMR spectra of Ure2p$_{1-89}$ fibrils, especially 2D spectra of uniformly ^{15}N,^{13}C-labeled fibrils, are qualitatively different from the corresponding spectra of HET-s$_{218-289}$ fibrils, as originally described by Seimer et al. (*50*, *51*) and confirmed under our own experimental conditions in Figure 6. The lower resolution in Ure2p$_{1-89}$ spectra is a consequence of greater structural disorder. ^{13}C NMR linewidths in Figure 4c are approximately 2.0 ppm, similar to linewidths observed in ^{13}C NMR spectra of Aβ_{1-40} fibrils, where linewidths of approximately 1.5 ppm for backbone sites are observed from hydrated samples with a single predominant fibril morphology (see Figure 7) and linewidths of 2.0−2.5 ppm are observed from lyophilized samples (*27*, *52*). The precise nature of structural disorder that leads to 2.0 ppm ^{13}C NMR linewidths is not known, but may include relatively minor variations in side chain and backbone torsion angles (approximately ±15°, sufficient to cause variations in conformation-dependent ^{13}C chemical shifts), variations in β-sheet twist, and variations in contacts between fibrils within fibril bundles. Major tertiary and quaternary structural variations, such as variations in the locations of β-strand and

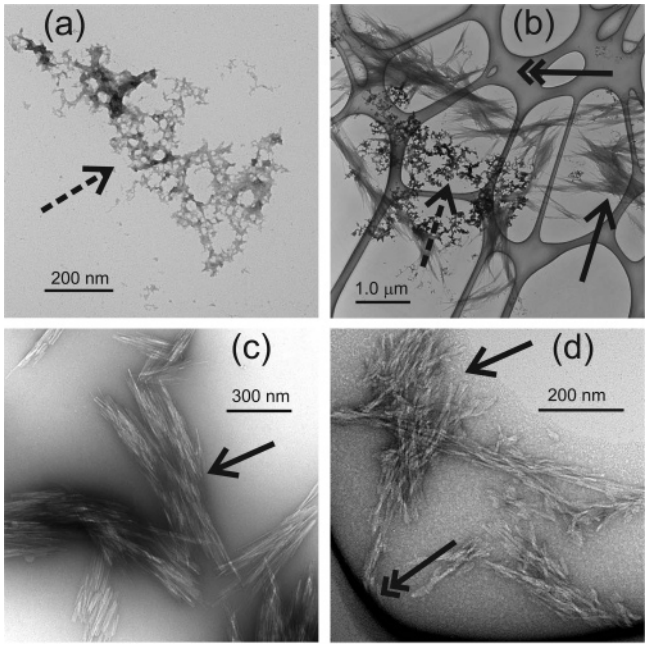

FIGURE 9: Representative TEM images of aggregated Ac-NNNNNNSSSNNNN-NH_2, negatively stained with uranyl acetate, obtained after 4 days of incubation in 10 mM phosphate buffer, pH 7.0, at 35 μM peptide concentration (a), 18 days of incubation at 140 μM peptide concentration (b), and 16 days of incubation at 560 μM peptide concentration (c). Image of aggregated Ac-QQQQQQSSSQQQQ-NH_2, obtained after 3 days in 6 M GdnHCl at 270 μM peptide concentration (d). Nonfibrillar and fibrillar aggregates are indicated by dashed and solid arrows, respectively. Double-headed arrow indicates the lacey carbon support of the electron microscope grid.

loop segments or variations in interstrand hydrogen-bonding patterns, are not required to produce 2.0 ppm linewidths, as shown by results for Aβ_{1-40} fibrils (*27*, *52*). On the other hand, the clear splitting of Ala15 cross peaks (regions 9 and 10 in Figure 4d) is a likely consequence of polymorphism, apparently involving the presence of Ala15 in β-strand and non-β-strand segments in two or more alternative Ure2p$_{1-89}$ fibril structures. Preparation of Ure2p$_{1-89}$ fibrils with a single predominant morphology, if experimentally achievable, might lead to improved resolution in 2D solid-state NMR spectra, but the existing data in Figures 4 and 5 (which show no evidence for sharp underlying peaks from specific morphologies) suggest that the improvement would be relatively minor.

As previously proposed (*42*, *50*), it appears likely that the high degree of structural order in HET-s$_{218-289}$ fibrils is a consequence of the evolved biological function of HET-s, as the determinant of heterokaryon incompatibility in *P. anserina* (reviewed in ref (*77*)). Data above show that a prion without an evolved biological function has a lower degree of structural order, similar to that in typical disease-associated amyloid fibrils. The amino acid sequence of HET-s$_{218-289}$ is also qualitatively different from the sequences of Sup35NM, Ure2p$_{1-89}$, and other amyloid-forming polypeptides, in that HET-s$_{218-289}$ contains only five Asn and two Gln residues and contains no hydrophobic segments longer than four residues. The structural model for HET-s$_{218-289}$ fibrils proposed by Ritter et al. (*42*) contains two layers of parallel β-sheet, with each molecule contributing two β-strands to each β-sheet and with alternation between intermolecular hydrogen bonding and intramolecular hydrogen bonding of β-strands within each β-sheet. This model for the β-sheet structure in HET-s$_{218-289}$ fibrils is consistent with recent electron microscopic determinations of the axial packing density of subunits in the fibril, which is half that observed in Ure2p fibrils, implying that they have basically different structures (*21*). In contrast, the parallel β-sheets in Ure2p$_{1-89}$ and Sup35NM fibrils contain only intermolecular hydrogen bonds. Ure2p$_{1-89}$ fibrils prepared *in vitro* produce an array of [URE3] strains when transformed into yeast (*8*). Distinct strains of the HET-s prion have not been reported.

ACKNOWLEDGMENT

We thank Dr. Wesley L. White for assistance with solution NMR spectroscopy of ^{13}C-labeled Ure2p$_{1-89}$. Amyloid fibril samples used for measurements in Figure 7 were prepared by Drs. Aneta T. Petkova, Anant K. Paravastu, Sorin Luca, and Gerd Buntkowsky. We thank Dr. Sven Saupe for providing the pET21a-Hets plasmid used in our production of HET-s$_{218-289}$.

SUPPORTING INFORMATION AVAILABLE

Full description of mass spectrometry and solution NMR measurements used to assess incorporation and scrambling of isotopic labels. Description of HET-s$_{218-289}$ expression and fibril formation. Raw fpRFDR-CT data (without natural-abundance ^{13}C corrections) for Ure2p$_{1-89}$ fibrils. This material is available free of charge via the Internet at http://pubs.acs.org.

REFERENCES

1. Taylor, K. L., Cheng, N. Q., Williams, R. W., Steven, A. C., and Wickner, R. B. (1999) Prion domain initiation of amyloid formation in vitro from native Ure2p, *Science 283*, 1339−1343.
2. Edskes, H. K., Gray, V. T., and Wickner, R. B. (1999) The [URE3] prion is an aggregated form of Ure2p that can be cured by overexpression of Ure2p fragments, *Proc. Natl. Acad. Sci. U.S.A. 96*, 1498−1503.
3. Masison, D. C., and Wickner, R. B. (1995) Prion-inducing domain of yeast Ure2p and protease resistance of Ure2p prion-containing cells, *Science 270*, 93−95.
4. Wickner, R. B. (1994) [URE3] as an altered Ure2 protein: Evidence for a prion analog in Saccharomyces cerevisiae, *Science 264*, 566−569.
5. Lacroute, F. (1971) Non-Mendelian mutation allowing ureidosuccinic acid uptake in yeast, *J. Bacteriol. 106*, 519-&.
6. Cooper, T. G. (2002) Transmitting the signal of excess nitrogen in Saccharomyces cerevisiae from the TOR proteins to the GATA factors: Connecting the dots, *FEMS Microbiol. Rev. 26*, 223−238.
7. Wickner, R. B., Edskes, H. K., Ross, E. D., Pierce, M. M., Baxa, U., Brachmann, A., and Shewmaker, F. (2004) Prion genetics: New rules for a new kind of gene, *Annu. Rev. Genet. 38*, 681−707.
8. Brachmann, A., Baxa, U., and Wickner, R. B. (2005) Prion generation in vitro: Amyloid of Ure2p is infectious, *EMBO J. 24*, 3082−3092.
9. Derkatch, I. L., Chernoff, Y. O., Kushnirov, V. V., IngeVechtomov, S. G., and Liebman, S. W. (1996) Genesis and variability of [PSI] prion factors in Saccharomyces cerevisiae, *Genetics 144*, 1375−1386.
10. King, C. Y., and Diaz-Avalos, R. (2004) Protein-only transmission of three yeast prion strains, *Nature 428*, 319−323.
11. Schlumpberger, M., Prusiner, S. B., and Herskowitz, I. (2001) Induction of distinct [URE3] yeast prion strains, *Mol. Cell. Biol. 21*, 7035−7046.
12. Tanaka, M., Chien, P., Naber, N., Cooke, R., and Weissman, J. S. (2004) Conformational variations in an infectious protein determine prion strain differences, *Nature 428*, 323−328.

13. Tanaka, M., Chien, P., Yonekura, K., and Weissman, J. S. (2005) Mechanism of cross-species prion transmission: An infectious conformation compatible with two highly divergent yeast prion proteins, *Cell 121*, 49−62.
14. Bousset, L., Belrhali, H., Janin, J., Melki, R., and Morera, S. (2001) Structure of the globular region of the prion protein Ure2 from the yeast Saccharomyces cerevisiae, *Structure 9*, 39−46.
15. Umland, T. C., Taylor, K. L., Rhee, S., Wickner, R. B., and Davies, D. R. (2001) The crystal structure of the nitrogen regulation fragment of the yeast prion protein Ure2p, *Proc. Natl. Acad. Sci. U.S.A. 98*, 1459−1464.
16. Baxa, U., Taylor, K. L., Wall, J. S., Simon, M. N., Cheng, N. Q., Wickner, R. B., and Steven, A. C. (2003) Architecture of Ure2p prion filaments: The N-terminal domains form a central core fiber, *J. Biol. Chem. 278*, 43717−43727.
17. Bai, M., Zhou, J. M., and Perrett, S. (2004) The yeast prion protein Ure2 shows glutathione peroxidase activity in both native and fibrillar forms, *J. Biol. Chem. 279*, 50025−50030.
18. Baxa, U., Speransky, V., Steven, A. C., and Wickner, R. B. (2002) Mechanism of inactivation on prion conversion of the Saccharomyces cerevisiae Ure2 protein, *Proc. Natl. Acad. Sci. U.S.A. 99*, 5253−5260.
19. Sunde, M., and Blake, C. C. F. (1998) From the globular to the fibrous state: Protein structure and structural conversion in amyloid formation, *Q. Rev. Biophys. 31*, 1−39.
20. Serpell, L. C., and Smith, J. M. (2000) Direct visualisation of the β-sheet structure of synthetic Alzheimer's amyloid, *J. Mol. Biol. 299*, 225−231.
21. Sen, A., Baxa, U., Simon, M. N., Wall, J. S., Sabate, R., Saupe, S. J., and Steven, A. C. (2007) Mass analysis by scanning transmission electron microscopy and electron diffraction validate predictions of stacked β-solenoid model of HET-s prion fibrils, *J. Biol. Chem. 282*, 5545−5550.
22. Oyler, N. A., and Tycko, R. (2004) Absolute structural constraints on amyloid fibrils from solid state NMR spectroscopy of partially oriented samples, *J. Am. Chem. Soc. 126*, 4478−4479.
23. Benzinger, T. L. S., Gregory, D. M., Burkoth, T. S., Miller-Auer, H., Lynn, D. G., Botto, R. E., and Meredith, S. C. (1998) Propagating structure of Alzheimer's β-amyloid(10−35) is parallel β-sheet with residues in exact register, *Proc. Natl. Acad. Sci. U.S.A. 95*, 13407−13412.
24. Gregory, D. M., Benzinger, T. L. S., Burkoth, T. S., Miller-Auer, H., Lynn, D. G., Meredith, S. C., and Botto, R. E. (1998) Dipolar recoupling NMR of biomolecular self-assemblies: Determining inter- and intrastrand distances in fibrilized Alzheimer's β-amyloid peptide, *Solid State Nucl. Magn. Reson. 13*, 149−166.
25. Shewmaker, F., Wickner, R. B., and Tycko, R. (2006) Amyloid of the prion domain of Sup35p has an in-register parallel β-sheet structure, *Proc. Natl. Acad. Sci. U.S.A. 103*, 19754−19759.
26. Chan, J. C. C., Oyler, N. A., Yau, W. M., and Tycko, R. (2005) Parallel β-sheets and polar zippers in amyloid fibrils formed by residues 10−39 of the yeast prion protein Ure2p, *Biochemistry 44*, 10669−10680.
27. Petkova, A. T., Ishii, Y., Balbach, J. J., Antzutkin, O. N., Leapman, R. D., Delaglio, F., and Tycko, R. (2002) A structural model for Alzheimer's β-amyloid fibrils based on experimental constraints from solid state NMR, *Proc. Natl. Acad. Sci. U.S.A. 99*, 16742−16747.
28. Balbach, J. J., Petkova, A. T., Oyler, N. A., Antzutkin, O. N., Gordon, D. J., Meredith, S. C., and Tycko, R. (2002) Supramolecular structure in full-length Alzheimer's β-amyloid fibrils: Evidence for a parallel β-sheet organization from solid state nuclear magnetic resonance, *Biophys. J. 83*, 1205−1216.
29. Antzutkin, O. N., Leapman, R. D., Balbach, J. J., and Tycko, R. (2002) Supramolecular structural constraints on Alzheimer's β-amyloid fibrils from electron microscopy and solid state nuclear magnetic resonance, *Biochemistry 41*, 15436−15450.
30. Antzutkin, O. N., Balbach, J. J., Leapman, R. D., Rizzo, N. W., Reed, J., and Tycko, R. (2000) Multiple quantum solid state NMR indicates a parallel, not antiparallel, organization of β-sheets in Alzheimer's β-amyloid fibrils, *Proc. Natl. Acad. Sci. U.S.A. 97*, 13045−13050.
31. Lansbury, P. T., Costa, P. R., Griffiths, J. M., Simon, E. J., Auger, M., Halverson, K. J., Kocisko, D. A., Hendsch, Z. S., Ashburn, T. T., Spencer, R. G. S., Tidor, B., and Griffin, R. G. (1995) Structural model for the β-amyloid fibril based on interstrand alignment of an antiparallel sheet comprising a C-terminal peptide, *Nat. Struct. Biol. 2*, 990−998.
32. Balbach, J. J., Ishii, Y., Antzutkin, O. N., Leapman, R. D., Rizzo, N. W., Dyda, F., Reed, J., and Tycko, R. (2000) Amyloid fibril formation by Aβ_{16-22}, a seven-residue fragment of the Alzheimer's β-amyloid peptide, and structural characterization by solid state NMR, *Biochemistry 39*, 13748−13759.
33. Petkova, A. T., Buntkowsky, G., Dyda, F., Leapman, R. D., Yau, W. M., and Tycko, R. (2004) Solid state NMR reveals a pH-dependent antiparallel β-sheet registry in fibrils formed by a β-amyloid peptide, *J. Mol. Biol. 335*, 247−260.
34. Gordon, D. J., Balbach, J. J., Tycko, R., and Meredith, S. C. (2004) Increasing the amphiphilicity of an amyloidogenic peptide changes the β-sheet structure in the fibrils from antiparallel to parallel, *Biophys. J. 86*, 428−434.
35. Bu, Z. M., Shi, Y., Callaway, D. J. E., and Tycko, R. (2007) Molecular alignment within β-sheets in Aβ_{14-23} fibrils: Solid state NMR experiments and theoretical predictions, *Biophys. J. 92*, 594−602.
36. Jaroniec, C. P., MacPhee, C. E., Bajaj, V. S., McMahon, M. T., Dobson, C. M., and Griffin, R. G. (2004) High-resolution molecular structure of a peptide in an amyloid fibril determined by magic angle spinning NMR spectroscopy, *Proc. Natl. Acad. Sci. U.S.A. 101*, 711−716.
37. Jaroniec, C. P., MacPhee, C. E., Astrof, N. S., Dobson, C. M., and Griffin, R. G. (2002) Molecular conformation of a peptide fragment of transthyretin in an amyloid fibril, *Proc. Natl. Acad. Sci. U.S.A. 99*, 16748−16753.
38. Griffiths, J. M., Ashburn, T. T., Auger, M., Costa, P. R., Griffin, R. G., and Lansbury, P. T. (1995) Rotational resonance solid state NMR elucidates a structural model of pancreatic amyloid, *J. Am. Chem. Soc. 117*, 3539−3546.
39. Benzinger, T. L. S., Gregory, D. M., Burkoth, T. S., Miller-Auer, H., Lynn, D. G., Botto, R. E., and Meredith, S. C. (2000) Two-dimensional structure of β-amyloid(10−35) fibrils, *Biochemistry 39*, 3491−3499.
40. Burkoth, T. S., Benzinger, T. L. S., Urban, V., Morgan, D. M., Gregory, D. M., Thiyagarajan, P., Botto, R. E., Meredith, S. C., and Lynn, D. G. (2000) Structure of the β-amyloid(10−35) fibril, *J. Am. Chem. Soc. 122*, 7883−7889.
41. Petkova, A. T., Yau, W. M., and Tycko, R. (2006) Experimental constraints on quaternary structure in Alzheimer's β-amyloid fibrils, *Biochemistry 45*, 498−512.
42. Ritter, C., Maddelein, M. L., Siemer, A. B., Luhrs, T., Ernst, M., Meier, B. H., Saupe, S. J., and Riek, R. (2005) Correlation of structural elements and infectivity of the HET-s prion, *Nature 435*, 844−848.
43. Iwata, K., Fujiwara, T., Matsuki, Y., Akutsu, H., Takahashi, S., Naiki, H., and Goto, Y. (2006) 3D structure of amyloid protofilaments of β_2-microglobulin fragment probed by solid state NMR, *Proc. Natl. Acad. Sci. U.S.A. 103*, 18119−18124.
44. Ferguson, N., Becker, J., Tidow, H., Tremmel, S., Sharpe, T. D., Krause, G., Flinders, J., Petrovich, M., Berriman, J., Oschkinat, H., and Fersht, A. R. (2006) General structural motifs of amyloid protofilaments, *Proc. Natl. Acad. Sci. U.S.A. 103*, 16248−16253.
45. Kammerer, R. A., Kostrewa, D., Zurdo, J., Detken, A., Garcia-Echeverria, C., Green, J. D., Muller, S. A., Meier, B. H., Winkler, F. K., Dobson, C. M., and Steinmetz, M. O. (2004) Exploring amyloid formation by a de novo design, *Proc. Natl. Acad. Sci. U.S.A. 101*, 4435−4440.
46. Edskes, H. K., and Wickner, R. B. (2002) Conservation of a portion of the s-cerevisiae Ure2p prion domain that interacts with the full-length protein, *Proc. Natl. Acad. Sci. U.S.A. 99*, 16384−16391.
47. Perutz, M. F., Johnson, T., Suzuki, M., and Finch, J. T. (1994) Glutamine repeats as polar zippers: Their possible role in inherited neurodegenerative diseases, *Proc. Natl. Acad. Sci. U.S.A. 91*, 5355−5358.
48. Nelson, R., Sawaya, M. R., Balbirnie, M., Madsen, A. O., Riekel, C., Grothe, R., and Eisenberg, D. (2005) Structure of the cross-β spine of amyloid-like fibrils, *Nature 435*, 773−778.
49. Ross, E. D., Baxa, U., and Wickner, R. B. (2004) Scrambled prion domains form prions and amyloid, *Mol. Cell. Biol. 24*, 7206−7213.
50. Siemer, A. B., Ritter, C., Steinmetz, M. O., Ernst, M., Riek, R., and Meier, B. H. (2006) ^{13}C,^{15}N resonance assignment of parts of the HET-s prion protein in its amyloid form, *J. Biomol. NMR 34*, 75−87.
51. Siemer, A. B., Ritter, C., Ernst, M., Riek, R., and Meier, B. H. (2005) High-resolution solid state NMR spectroscopy of the prion protein HET-s in its amyloid conformation, *Angew. Chem., Int. Edit. 44*, 2441−2444.

52. Petkova, A. T., Leapman, R. D., Guo, Z. H., Yau, W. M., Mattson, M. P., and Tycko, R. (2005) Self-propagating, molecular-level polymorphism in Alzheimer's β-amyloid fibrils, *Science 307*, 262−265.
53. Tycko, R. (2006) Molecular structure of amyloid fibrils: Insights from solid state NMR, *Q. Rev. Biophys. 39*, 1−55.
54. Blanco, F. J., Hess, S., Pannell, L. K., Rizzo, N. W., and Tycko, R. (2001) Solid state NMR data support a helix-loop-helix structural model for the n-terminal half of HIV-1 Rev in fibrillar form, *J. Mol. Biol. 313*, 845−859.
55. Cai, M. L., Huang, Y., Sakaguchi, K., Clore, G. M., Gronenborn, A. M., and Craigie, R. (1998) An efficient and cost-effective isotope labeling protocol for proteins expressed in Escherichia coli, *J. Biomol. NMR 11*, 97−102.
56. Ishii, Y., Balbach, J. J., and Tycko, R. (2001) Measurement of dipole-coupled lineshapes in a many-spin system by constant-time two-dimensional solid state NMR with high-speed magic-angle spinning, *Chem. Phys. 266*, 231−236.
57. Petkova, A. T., and Tycko, R. (2002) Sensitivity enhancement in structural measurements by solid state NMR through pulsed spin locking, *J. Magn. Reson. 155*, 293−299.
58. Ishii, Y. (2001) ^{13}C-^{13}C dipolar recoupling under very fast magic angle spinning in solid state nuclear magnetic resonance: Applications to distance measurements, spectral assignments, and high-throughput secondary-structure determination, *J. Chem. Phys. 114*, 8473−8483.
59. Wishart, D. S., Bigam, C. G., Yao, J., Abildgaard, F., Dyson, H. J., Oldfield, E., Markley, J. L., and Sykes, B. D. (1995) ^{1}H, ^{13}C, and ^{15}N chemical shift referencing in biomolecular NMR, *J. Biomol. NMR 6*, 135−140.
60. Delaglio, F., Grzesiek, S., Vuister, G. W., Zhu, G., Pfeifer, J., and Bax, A. (1995) NMRpipe: A multidimensional spectral processing system based on Unix pipes, *J. Biomol. NMR 6*, 277−293.
61. Wishart, D. S., Bigam, C. G., Holm, A., Hodges, R. S., and Sykes, B. D. (1995) ^{1}H, ^{13}C, and ^{15}N random coil NMR chemical shifts of the common amino acids. 1. Investigations of nearest-neighbor effects, *J. Biomol. NMR 5*, 67−81.
62. Saito, H. (1986) Conformation-dependent ^{13}C chemical-shifts: A new means of conformational characterization as obtained by high-resolution solid state ^{13}C NMR, *Magn. Reson. Chem. 24*, 835−852.
63. Wylie, B. J., Sperling, L. J., Frericks, H. L., Shah, G. J., Franks, W. T., and Rienstra, C. M. (2007) Chemical shift anisotropy measurements of amide and carbonyl resonances in a microcrystalline protein with slow magic-angle spinning NMR spectroscopy, *J. Am. Chem. Soc. 128*, 5318−5319.
64. Lührs, T., Ritter, C., Adrian, M., Riek-Loher, D., Bohrmann, B., Döbeli, H., Schubert, D., and Riek, R. (2005) 3D structure of Alzheimer's amyloid-β(1−42) fibrils, *Proc. Natl. Acad. Sci. U.S.A. 102*, 17342−17347.
65. Paravastu, A. K., Petkova, A. T., and Tycko, R. (2006) Polymorphic fibril formation by residues 10−40 of the Alzheimer's β-amyloid peptide, *Biophys. J. 90*, 4618−4629.
66. Heise, H., Hoyer, W., Becker, S., Andronesi, O. C., Riedel, D., and Baldus, M. (2005) Molecular-level secondary structure, polymorphism, and dynamics of full-length α-synuclein fibrils studied by solid state NMR, *102*, 15871−15876.
67. Siemer, A. B., Arnold, A. A., Ritter, C., Westfeld, T., Ernst, M., Riek, R., and Meier, B. H. (2006) Observation of highly flexible residues in amyloid fibrils of the HET-s prion, *J. Am. Chem. Soc. 128*, 13224−13228.
68. Santoso, A., Chien, P., Osherovich, L. Z., and Weissman, J. S. (2000) Molecular basis of a yeast prion species barrier, *Cell 100*, 277−288.
69. Perutz, M. F., Pope, B. J., Owen, D., Wanker, E. E., and Scherzinger, E. (2002) Aggregation of proteins with expanded glutamine and alanine repeats of the glutamine-rich and asparagine-rich domains of Sup35 and of the amyloid β-peptide of amyloid plaques, *Proc. Natl. Acad. Sci. U.S.A. 99*, 5596−5600.
70. Jenkins, J., and Pickersgill, R. (2001) The architecture of parallel β-helices and related folds, *Prog. Biophys. Mol. Biol. 77*, 111−175.
71. Jayasinghe, S. A., and Langen, R. (2004) Identifying structural features of fibrillar islet amyloid polypeptide using site-directed spin labeling, *J. Biol. Chem. 279*, 48420−48425.
72. Margittai, M., and Langen, R. (2004) Template-assisted filament growth by parallel stacking of tau, *Proc. Natl. Acad. Sci. U.S.A. 101*, 10278−10283.
73. Der-Sarkissian, A., Jao, C. C., Chen, J., and Langen, R. (2003) Structural organization of α-synuclein fibrils studied by site-directed spin labeling, *J. Biol. Chem. 278*, 37530−37535.
74. Torok, M., Milton, S., Kayed, R., Wu, P., McIntire, T., Glabe, C. G., and Langen, R. (2002) Structural and dynamic features of Alzheimer's Aβ peptide in amyloid fibrils studied by site-directed spin labeling, *J. Biol. Chem. 277*, 40810−40815.
75. Kajava, A. V., Baxa, U., Wickner, R. B., and Steven, A. C. (2004) A model for Ure2p prion filaments and other amyloids: The parallel superpleated β-structure, *Proc. Natl. Acad. Sci. U.S.A. 101*, 7885−7890.
76. Kajava, A. V., Aebi, U., and Steven, A. C. (2005) The parallel superpleated β-structure as a model for amyloid fibrils of human amylin, *J. Mol. Biol. 348*, 247−252.
77. Saupe, S. J., Clave, C., and Begueret, J. (2000) Vegetative incompatibility in filamentous fungi: Podospora and neurospora provide some clues, *Curr. Opin. Microbiol. 3*, 608−612.

BI700826B